Fiber Field-Effect Device via *In-Situ* Channel Crystallization

Academic and research staff
Sylvain Danto, Fabien Sorin, Nicholas D. Orf, Zheng Wang, John D. Joannopoulos, Yoel Fink

Sponsor
DARPA, ISN, DOE, NSF

The fabrication of metal-insulator-semiconductor fiber structures has been limited to the use of amorphous semiconductors, which exhibit inferior electronic transport properties compared to their crystalline counterparts. Here, for the first time, we demonstrate that the competing requirements for thermal drawing and subsequent phase-change in amorphous semiconductors can be reconciled to incorporate *crystalline semiconductors* into multimaterial fibers. Using this technique, we present the first arbitrarily long s*ingle-fiber* field-effect device.

To demonstrate the post-drawing thermal crystallization scheme, we fabricate fiber constituted of a solid-core $As_{40}Se_{52}Te_8$ chalcogenide glass in intimate contact with four Sn electrodes that extend the full length of the fibre and surrounded with a polymeric PES cladding. Samples are subsequently annealed at 208 °C and characterized at regular period of time. In Figure 1, we compare XRD patterns (panel a) and DSC measurements (panel b) of samples annealed for 0 and 24 days. The XRD pattern of the as-drawn fiber shows halos of diffraction typical of an amorphous material (Figure 1a). In contrast, the XRD pattern of the annealed fiber shows a superposition of diffuse halos and sharp crystallographic peaks typical of a glass-ceramic. Peak indexation verifies the presence of a crystalline phase isostructural to monoclinic α-$As_{40}Se_{60}$. The SEM micrograph also reveal that the growth of the crystalline phase inside the $As_{40}Se_{52}Te_8$ region begins at the glass' interfaces with the electrodes and polymer cladding and extends into the bulk (Figure 1a inset). The partial crystallization of the semiconductor is further supported by DSC measurements (Figure 1b). In Figure 1b (top), the unannealed glass exhibits a single characteristic temperature at T_g = 165 °C while the annealed glass shows an additional melting peak at T_m = 338 °C, suggesting a crystalline phase exists within the glassy matrix. In Figure 1b (bottom), DSC scans of complete sections of both as-drawn and annealed fibers show the characteristic thermal parameters of the three constituting components (T_g $As_{40}Se_{52}Te_8$ = 165 °C, T_g PES = 225 °C, T_m Sn = 232 °C). The annealed fiber exhibits an additional endothermic peak at 338 °C, matching exactly with the melting temperature of the crystalline $As_{40}Se_{52}Te_8$ phase. *In-situ* crystallization drastically reduces the density of localized states inside the band-gap of the semiconductor and hence increases carrier mobility, allowing active electric devices to be constructed. As a proof of concept, we demonstrate a *single-fiber* p-channel field-effect device. The structure consists of two identical thin film devices, each made of the p-type $As_{40}Se_{52}Te_8$ semiconductor functioning as the channel and contacted by two parallel Sn electrodes acting as the source and the drain (Figure 2a). A third Sn electrode is used as the gate and is separated from the channel by a PES dielectric layer. A fiber device, designed to operate in accumulation mode, was prepared and annealed at 208 °C. After annealing for 14 days, the source-to-drain current I_{DS} shows a strongly nonlinear dependence on the applied gate voltage V_G under fixed V_{DS} (Figure 2 top). In contrast, identical non-annealed fiber structures yield extremely low channel conductivity and no dependence on the gate voltage. In Figure 2b (bottom), the source-to-drain current - voltage characteristics demonstrate a clear increase in the conductance of the channel as the gate bias is varied from 0 V to -100 V. A clear current modulation in the crystalline devices is demonstrated revealing an unpinned Fermi level not achievable in the amorphous state that results from a transition towards a more ordered structure. Although underestimated due to the effect of contact resistance, the mobility of the c-$As_{40}Se_{52}Te_8$ semiconductor in the FET device is found to be ~1.50 10^{-2} cm^2 V^{-1} s^{-1}, a substantial increase over the amorphous state ($\mu_{a\text{-}As2Se3}$ ~5.00 10^{-5} cm^2 V^{-1} s^{-1}).

Here we demonstrate the integration of a phase-changing glassy semiconductor compatible with thermal drawing inside a fiber and we present a fiber field-effect device fabricated via the *in-situ*

crystallization of the channel. It will serve as a building block for large-scale fiber-integrated digital circuits, paving the way towards optoelectronic and logic operations in polymer fibers and fabrics.

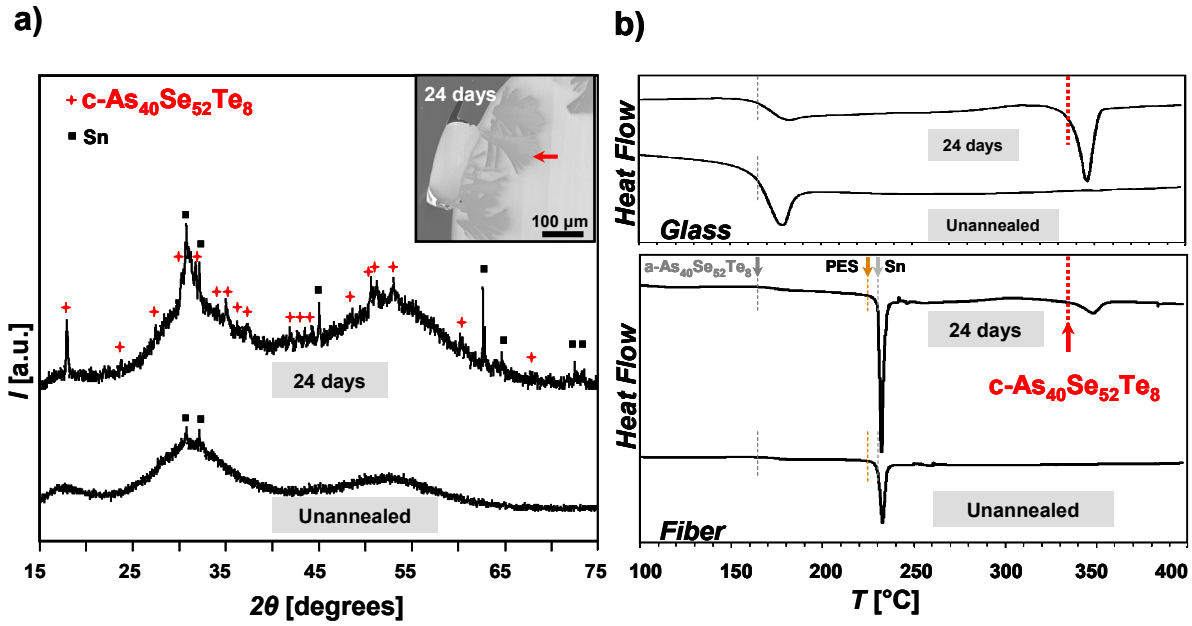

Figure 1. Characterization of crystalline semiconductor domains. **a)** XRD patterns of unannealed and annealed (24 days) fibers. A crystalline phase (c-$As_{40}Se_{52}Te_8$) isostructural to α-$As_{40}Se_{60}$ grows inside the glassy matrix with extended annealing (inset: SEM micrograph of a fiber cross-section annealed for 24 days, red arrow highlight crystalline domains). **b)** DSC scans of $As_{40}Se_{52}Te_8$ glass (top) and multimaterial fiber (bottom). Annealing of both glass and fiber for 24 days leads to the presence of an exothermal peak at T_m = 338 °C associated with the melting of crystalline $As_{40}Se_{52}Te_8$.

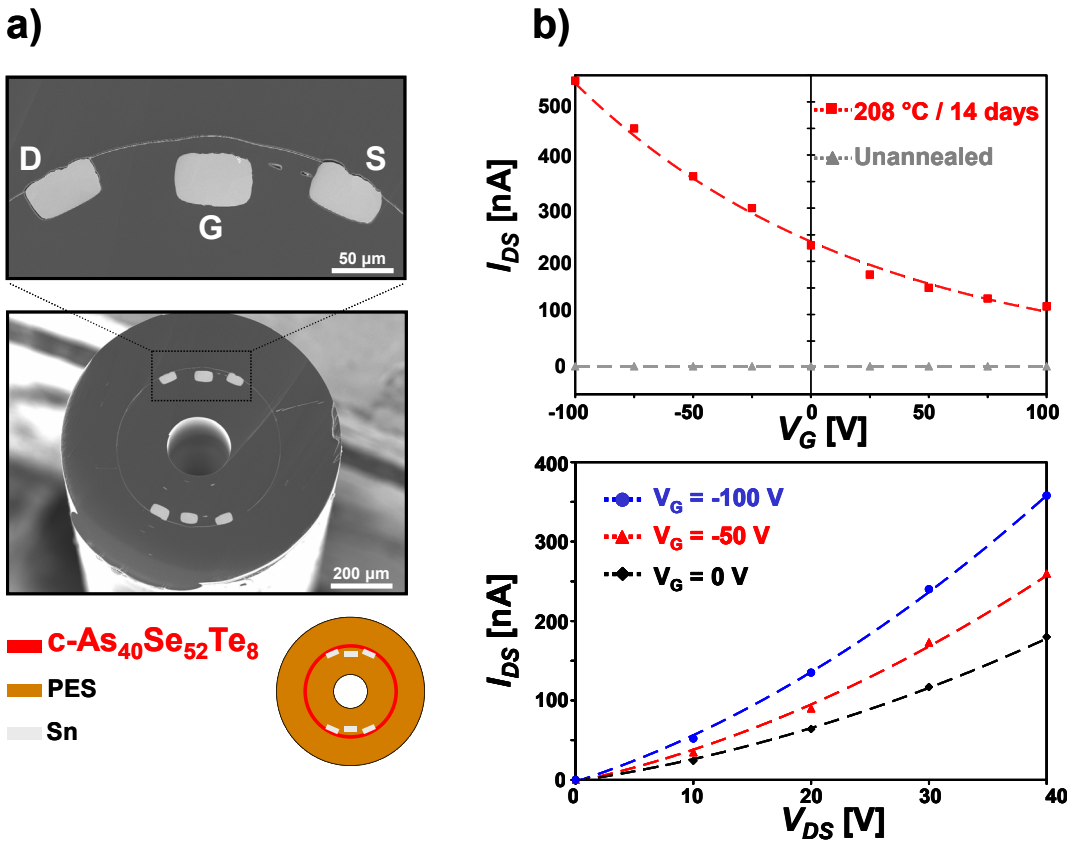

Figure 2. Fiber p-channel field-effect device. **a)** SEM micrographs of the cross-section of the fiber device whole structure (bottom). Magnification of one of the two devices (top) (G: Gate, D: Drain, S: Source). Two parallel source and drain Sn electrodes are in contact with the p-type $As_{40}Se_{52}Te_8$ film. A third Sn electrode separated from the channel by an insulating PES polymer film functions as the gate electrode. **b)** Characterization of the field-effect device. Change of drain-to-source current ΔI_{DS} as a function of the gate voltage V_G for unannealed and 14 days annealed fibers (V_{DS} = *20 V*) (top). Source-to-drain I_{DS} – V_{DS} characteristics of the field-effect device as function of the gate voltage (bottom).

Enabling coherent superpositions of iso-frequency optical states in multimode fibers

Participants:
Ofer Shapira, Dana Shemuly, John D. Joannopoulos, and Yoel Fink

Funding:
NSF/MRSEC, US Army

The ability to precisely and selectively excite superpositions of specific fiber eigenmodes allows one in principle to control the three dimensional field distribution along the length of a fiber. Here we demonstrate the dynamic synthesis and controlled transmission of vectorial eigenstates in a hollow core cylindrical photonic bandgap fiber, including a coherent superposition of two different angular momentum states. The results are verified using a modal decomposition algorithm that yields the unique complex superposition coefficients of the eigenstate space.

Waveguides supporting a multiplicity of iso-frequency states are characterized by an entropic increase in the population of states due to axially distributed perturbations. Initiating and maintaining a specific population through a controlled excitation and transmission of coherent superposition of eigenstates in a “constant entropy” regime can be highly desirable. The

motivation is twofold. First, the formation of three dimensional field distributions can be achieved along the longitudinal dimension of a fiber providing a new medium for controlled light matter interactions. Second, the larger modal area and the controlled excitation could enable high-power lasers and waveguides to operate in higher energies without compromising the beam quality. Here we introduce an approach to synthesize, controllably transmit, and analyze coherent superpositions of fiber eigenmodes beyond the traditional single mode excitation. We show that in fact one may produce coherent linear superpositions of iso-frequency vectorial modes with different angular momenta and control their weights in real time.

Controlling the eigenstate population of multimode waveguides enables the introduction of a characteristic axial length scale even in photonic structures that have complete axial translation symmetry. The length scale is associated with the spatial mode beating between non-degenerate iso-frequency modes and can be tailored by a proper choice of the expansion coefficients of the eigenstate superposition. Figure 1 depicts a cross section of such fiber and an intensity pattern of a coherent superposition of four low-energy modes of such fiber demonstrating the ability to form periodic patterns inside the hollow core. To demonstrate this approach, a cylindrically symmetric hollow-core photonic band gap fiber with core diameter of 68 μm (Fig. 1a) was drawn using the preform-based fabrication method [14-16]. Such fiber supports several thousands of vectorial leaky-modes by confining light in the hollow core region via omnidirectional reflection from the cylindrically symmetric multilayer structure lining the core [17,18].

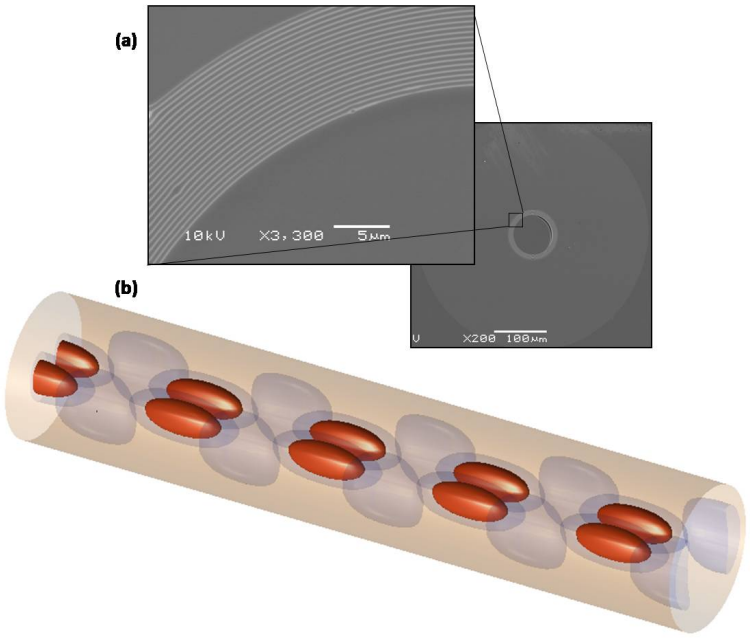

Fig. 1 (a) Scanning electron microscope micrographs of a multilayer cylindrically symmetric photonic band gap fiber cross section with a core diameter of 68 μ m. (b) Three dimensional intensity distribution of a coherent superposition of four low energy eigenstates of the fiber. The red and blue regions correspond to surfaces in which the intensity drops to 1/4 and 1/16 of its maximal value, correspondingly.

The optical setup involved a linearly polarized laser beam at 1.5 that impinges normally on a reflective SLM through a beam splitter and then reflects back to a lens that couples the beam to the fiber. The SLM imparts a computer-controlled phase distribution to the optical wave front. Applying the constant phase distribution to the SLM results in strong coupling to the HE_{11} (Fig. 2a) while by dividing the screen to two halves and applying a π phase different between them results in coupling to the azimuthally polarized, donut shaped, low loss TE_{01} mode.

While it may be possible to identify visually some of the simpler low-order modes, the same is not possible when the beam is a superposition of such modes. In such cases a distinct approach is required that reliably decomposes the output beam into its constituent modes revealing the relative (complex) contribution of each eigenmode. We previously developed a non-interferometric approach to achieve modal decomposition of the fields at the output of a general waveguide [6]. To demonstrate the excitation and transmission of a coherent superposition of these two modes we varied the phase of one half of the phase image from 0 to π while keeping the other half fixed to 0. For each value of the super position weight, *a,* we acquired the relevant intensity images. We applied the mode decomposition algorithm for each set and obtained the complex coefficients of the first 12 lowest energy modes with *m*<3 (Fig. 2c). Examples of the acquired far-field intensity images for *a*=0.625 are shown in Fig. 2b.

This ability to control the eigenstates population provides a mean to determine and tailor the three dimensional field distribution along the fiber axis. Fig. 2d shows the time averaged intensity distribution of $\left|\Psi_S\right|^2$. This result demonstrates the ability to construct a volumetric intensity (and field) patterns inside the fiber from knowledge of the complex expansion coefficients through control excitation of eigenstates at the input and verification of the modal content at the output of a waveguide.

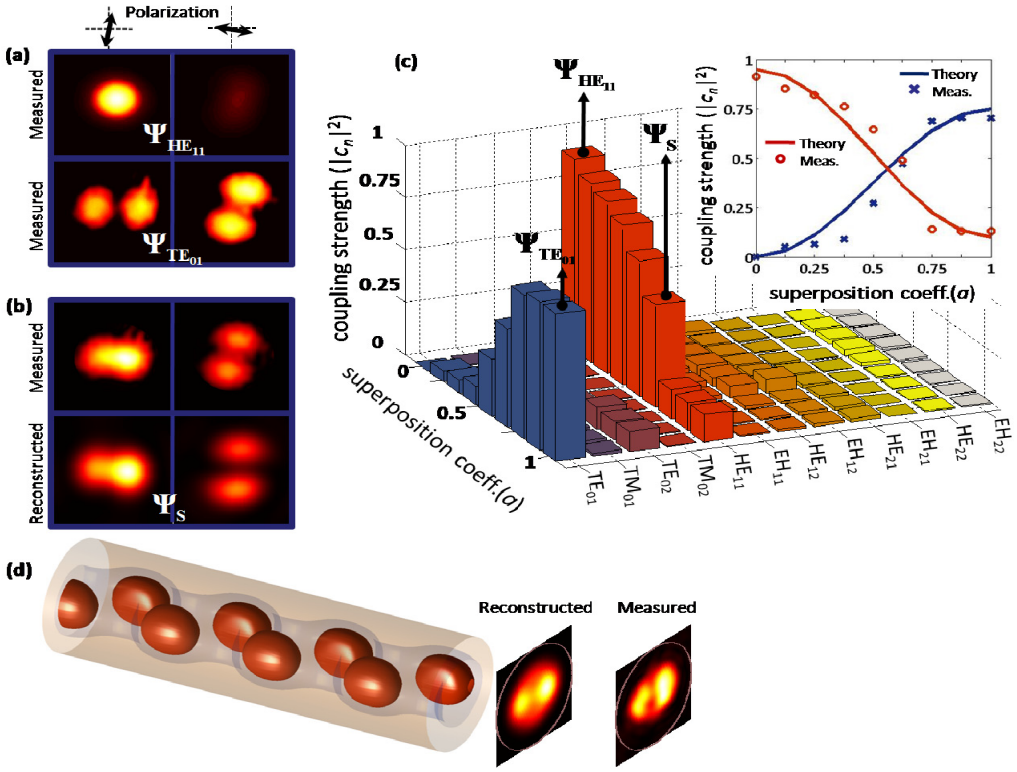

Fig. 2 (a) Measured intensity distribution for two perpendicular polarizations of the HE_{11} (upper panel) and TE_{01} (lower panel). (b) Far-field intensity patterns of the measured (upper panel) and reconstructed (lower panel) superposition of the two modes for a=0.625. (c) Coupling strength of the different modes as obtained from the mode decomposition algorithm for several values of the superposition coefficient *a*. The inset shows consolidated results for the main two modes together with theoretical calculation of the expected coupling coefficients. (d) Three-dimensional time averaged intensity pattern of the superposition defined by a=0.625.

[1] B. Temelkuran, S.D. Hart, G. Benoit, J.D. Joannopoulos, and Y. Fink, Nature **20**, 650-653 (2002).
[2] K. Kuriki, O. Shapira, S.D. Hart, G. Benoit, Y. Kuriki, J.F. Viens, M. Bayindir, J.D. Joannopoulos, and Y. Fink, Opt. Express **12**, 1510-1517, (2004).
[3] O. Shapira, K. Kuriki, N.D. Orf, A.F. Abouraddy, G. Benoit, J.F. Viens, M.M. Brewster, A. Rodriguez, M. Ibanescu, J.D. Joannopoulos, and Y. Fink, Opt. Express **14**, 3929-3935 (2006).
[4] S. Johnson, M. Ibanescu, M. Skorobogatiy, O. Weisberg, T. Engeness, M. Soljacic, S. Jacobs, J.D. Joannopoulos, and Y. Fink, Optics Express, **9**, 13 (2001).
[5] J.D. Joannopoulos, S.G. Johnson, J.N. Winn, and R.D. Meade, *Photonic Crystals* (Princeton University Press 2008).
[6] O. Shapira, A.F. Abouraddy, J.D. Joannopoulos, and Y. Fink, Phys. Rev. Lett. **94**, 143902 (2005).

Numerical simulation of capillary instability in a concentric-cylindrical shell

Academic and research staff
Daosheng Deng, Dr. Jean-Christophe Nave, Professor Steven G. Johnson, Professor Yoel Fink

Sponsors
ISN, MRSEC

A new class of microstructured fibers, which are characterized by an embedded geometry of concentric cylindrical shells, has emerged [1]. Uniform-thickness cylindrical shells, down to sub-micrometer scales, have been successfully fabricated by a thermal drawing process. As the thickness is further reduced towards the nanoscale, however, the thin cylindrical shell evolves into an ordered array of filaments [2]. To understand these observations, we explore whether a classical capillary instability, as a fundamental physical mechanism, is relevant to the lower limit of feature size in our fibers.

The govern equations of capillary instability in the simulation is the full Navier-Stokes equations

$$\begin{cases} \rho\left(\partial_t u + (u\cdot\nabla)u\right) = -\nabla p + \eta\nabla^2 u - \gamma\kappa n\delta, \\ \nabla\cdot u = 0, \end{cases}$$

where η is viscosity, γ, interfacial tension, and ρ, density; δ is a delta function at interface, and, κ curvature of interface. A level set function (ϕ) is applied to track the interface $\phi_t + u\cdot\nabla\phi = 0$.

Our simulation algorithm is briefly presented in Fig. 1(a). Geometry of a cylindrical shell is defined by two interfaces *I, II* in Fig. 1(b). Flow field is calculated from Navier-Stokes equations, as seen in Fig. 1(c). Consequently, this new flow field generates interface motion, resulting in an updated interface and flow field. By these numerical iterations, interface gradually evolves with time.

A radial stability map, as shown in Fig.2, is established to identify the regime in which our fiber drawing is operating [3]. Feature size down to submicrometers of materials combination *As_2Se_3-PES* is stable, which is consistent with our necessary criterion of radial stability because these viscosities $\eta_{clad}=\eta_{shell}= 10^5$pa·s together with radius r= 500 μm fall into the stable region. Uniform layer thickness at submicrometer scale is attributed to high viscosity and large radius. The radial stability criterion, nevertheless, is not a sufficient condition to predict the stable cylindrical shells in our microstructured fibers, since azimuthal instability of layers occurs at further reduced thickness down to nanometers.

This radial stability map can usefully exclude reasonable-sounding material combinations from consideration, which analysis predicts would be unstable. For example, materials combination of *Se-PE*, which has viscosities $\eta_{shell}= 10$, $\eta_{clad}= 10^3$ pa·s, falls into unstable or axial-breakup region and is not a good candidate for our fiber drawing. This work offers theoretical guidance to

rationally choose suitable material combinations and optimally control process in materials science and nanostructure fabrication.

References

[1] A. F. Abouraddy, M. Bayindir, G. Benoit, S. D. Hart, K. Kuriki, N. Orf, O. Shapira, F. Sorin, B. Temelkuran, Y. Fink, Towards multimaterial multifunctional fibres that see, hear, sense and communicate, *Nature Materials* **6,** 336 (2007).

[2] D. S. Deng, N. D. Orf, A. F. Abouraddy, A. M. Stolyarov, J. D. Joannopoulos, H. A. Stone, and Y. Fink, In-fiber semiconductor filament arrays, *Nano Letters* **8,** 4265, (2008).

[3] D. S. Deng, J. C. Nave, S. G. Johnson, and Y. Fink, Capillary instability in concentric-cylindrical shell: numerical simulation and application in microstructured fibers (in preparation).

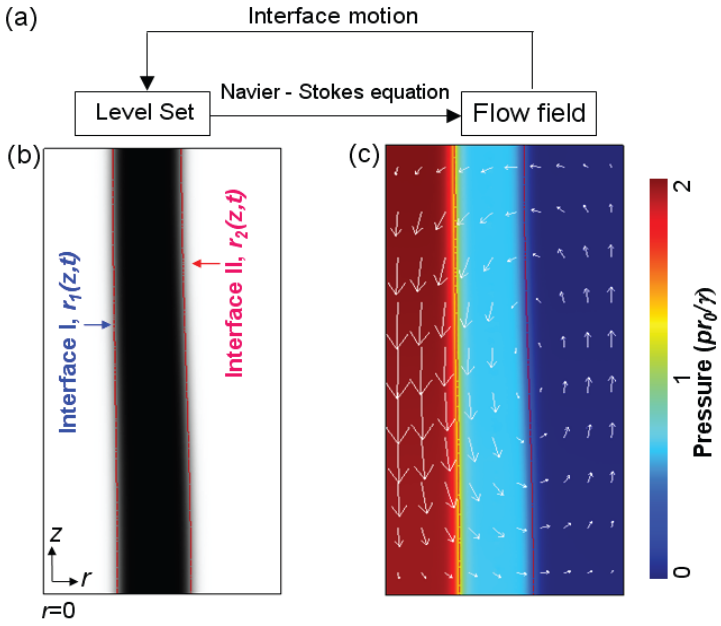

Figure 1 Simulation algorithm. (a) Chart of algorithm. (b) Interface *I* and *II* of cylindrical shell is defined by the level set function, which evolves with flow field. (c) Flow field is determined by the NS equations. Dark color for cylindrical shell region in (b); color scale for pressure and arrows for fluid velocity in (c).

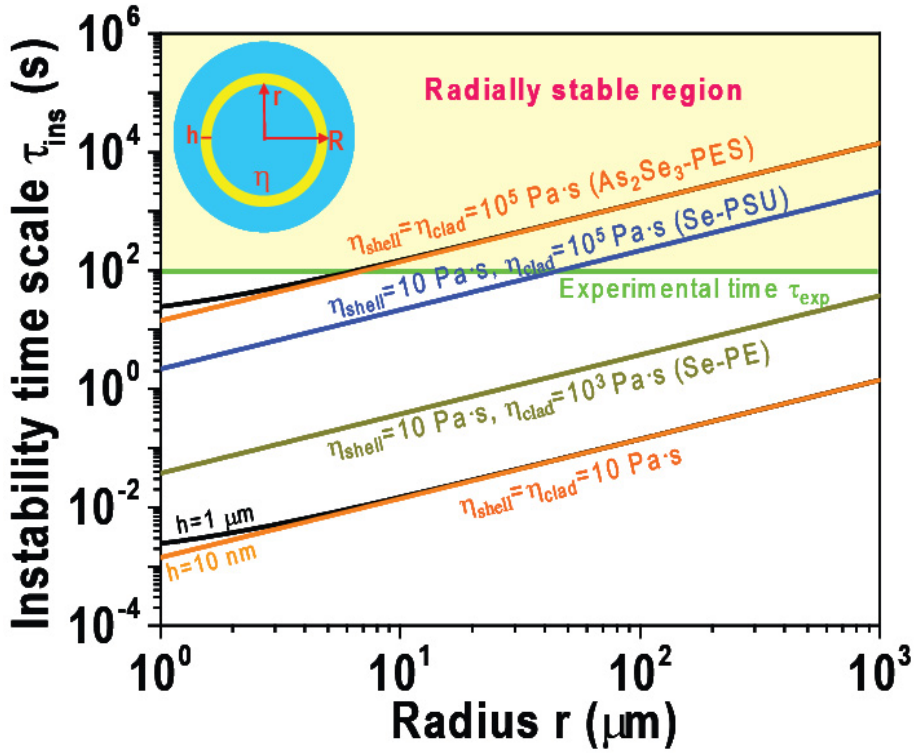

Figure 2 Radial stability map. Linear theory calculations of instability time scale dependent of the radius, thickness, and viscosity. Experimental time scale of thermal drawing around τ_{exp} ~ 100 sec, and fiber radius r ~ 500μm. Inset shows the cross-sectional geometry of cylindrical shell. Radially stable region for $\tau_{ins} > \tau_{exp}$, while unstable region for $\tau_{ins} < \tau_{exp}$.

Piezoelectric fibers for acoustic sensing and actuation

Project Staff
Shunji Egusa, Zheng Wang, Noémie Chocat, Zach M. Ruff, A. M. Stolyarov, Dana Shemuly, Fabien Sorin, Peter T. Rakich, John D. Joannopoulos, Yoel. Fink

Sponsors
ARO, DARPA, ISN, NSF

Throughout the evolution of fibers, from the ancient textile yarns to modern fiber-optic communication systems, a key premise has remained unchanged – that fibers are essentially static, incapable of controllably changing their properties at arbitrary frequencies. Unique opportunities would arise if a rapid electrically-driven mechanism for changing fiber properties existed. Hence a wide spectrum of hitherto static fiber devices could at once become tunable with applications spanning electronics, mechanics, acoustics, and optics, with the benefits of large surface-area, structural robustness, and mechanical flexibility (1). A number of studies have demonstrated the possibility to change fiber properties dynamically through mechanical stress, temperature changes or electric fields over short lengths of fiber notably using non-linear optical effects (2-8).

One intriguing path for introducing rapid modulation into fibers would be through the piezoelectric effect (9, 10). Embedding piezoelectric domains would allow fibers to be electrically actuated over broad frequencies on the one hand, and to function as sensitive broadband microphones on the other. A reasonable approach would first involve the construction of a large perform made of a piezoelectric material poly(vinylidene fluoride) (PVDF) (11-13), with metal electrodes and an insulating polymer, followed by a subsequent thermal draw. The stress present during the fiber draw should induce the non-polar α to ferroelectric β phase transition in the PVDF layer (13-16). The process should yield many meters of fiber with internal electrodes which could be utilized to establish the large electric field necessary for poling the PVDF layer. However, upon detailed examination a number of significant challenges and seemingly conflicting tendencies arise. The necessity to utilize crystalline materials both for the piezoelectric layer and the electrical conductors leads to the formation of multiple adjacent low viscosity domains. These domains undergoing a reduction in cross section dimensions are susceptible to capillary breakup and mixing during fiber drawing due to flow instabilities. This results in dimensional fluctuations both in the lateral and longitudinal directions (17, 18). These in turn preclude the formation of the coercive field needed for poling. Moreover, even if capillary breakup was kinetically averted and uniform sections of fibers were to emerge they would not exhibit piezoelectricity because the stress and strain conditions necessary to induce the thermodynamic phase transition in PVDF cannot be sustained in the fiber draw process.

To address these challenges we choose to initially focus our attention on the ability to maintain geometric coherence and uniformity. A viscous and conductive carbon loaded poly(carbonate) (CPC) is used to confine the low viscosity piezoelectric layer. The CPC layers combine high viscosity and adequate conductivity over the frequency range from DC to tens of MHz. Thus the CPC facilitates short range (hundreds of microns) charge transport on length scales associated with the fiber cross section. Once the geometry and charge transport issues are addressed we then proceed to identify a piezoelectric polymer which crystallizes into the appropriate phase. Poly(vinylidene-fluoride-Trifluoroethylene) copolymer (P(VDF-TrFE)) (19) assumes the ferroelectric β phase spontaneously upon solidification from the melt (20, 21) without necessitating any mechanical stress making it particularly suitable for the thermal fiber drawing process.

With the fiber materials selected, we proceed to elaborate a fabrication process which is illustrated in Figure 1A. A series of shells comprising 700 μm-thick layer of P(VDF-TrFE) (70:30 molar ratio, Solvey; melt-pressed from pellets) and 250 μm–thick layer of CPC are assembled with indium filaments and a poly(carbonate) (PC) cladding. The entire structure is consolidated at

210°C to remove trapped gas and form high quality interfaces. The preform is then thermally drawn in a furnace at 230°C into fibers. Scanning electron microscopy (SEM) images of the fiber cross section show the P(VDF-TrFE) layer (40 μm thick) sandwiched between CPC layers, with the shape and the aspect ratio unchanged from those of the preform (Figure 1B). Wide angle X-ray diffraction (XRD) measurements of P(VDF-TrFE) copolymer domains harvested from the drawn fibers, are compared to the material used for the performs. Both specimen exhibit identical peaks at 2θ = 19.9, 35.2, and 40.7 degrees, which correspond to (200)/(110), (001) and (310)/(020), (111)/(201) and (400)/(220) peaks of the β phase (22) respectively (Figure 1C), thus establishing that the drawn copolymer solidifies in its β phase. The crystallinity fraction as calculated from XRD patterns is over 90%. The obtained fiber is then poled by applying through the internal fiber electrodes an electric field in excess of 60 MV/m which is above the literature value (23) of coercive fields. Long lengths of fibers are readily poled in this way.

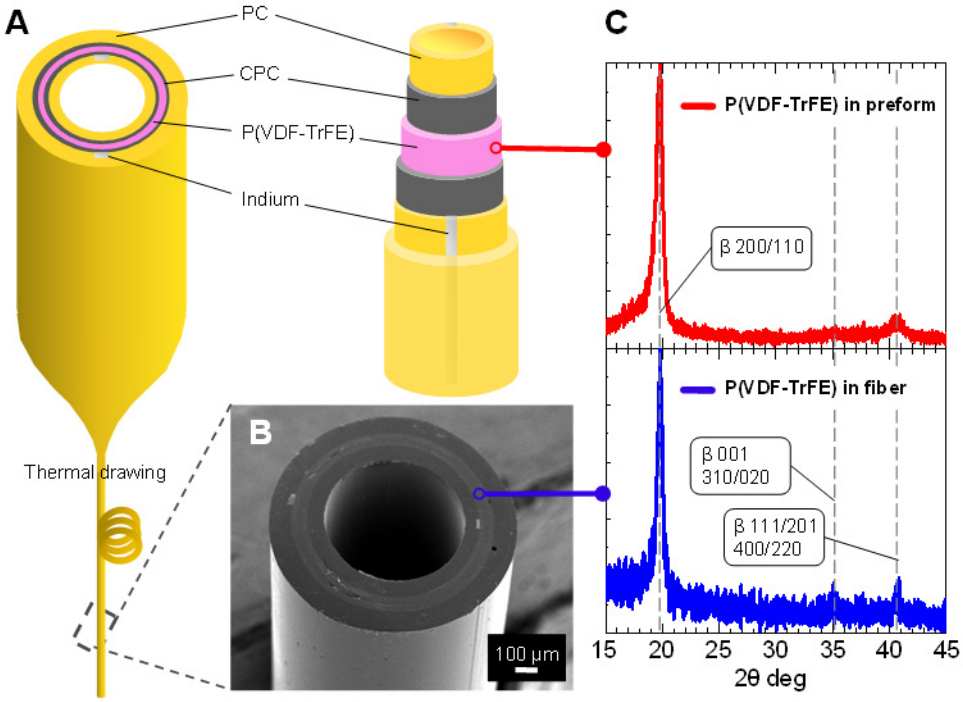

Figure 1 (A) Schematic of the fabrication process of a cylindrical piezoelectric fiber. A preform is constructed by consolidating a shell of P(VDF-TrFE), shells containing CPC/indium electrodes, and PC cladding. (B) SEM micrograph of the cross section of a cylindrical piezoelectric fiber. (C) XRD patterns of P(VDF-TrFE) samples extracted from drawn fibers and taken from melt-pressed films used in the preforms. The diffraction peaks indicate β-phase P(VDF-TrFE).

Heterodyne optical interferometry (24, 25) is used to probe the surface vibration of fibers driven by external electrical signals. The experimental setup (Figure 2A) consists of a frequency-swept (1530 – 1570 nm, at 80 nm/s) laser (Agilent Technologies, 8164B) coupled to a fiber-optic Michelson interferometer and a Fabry-Perot frequency reference. The fiber sample is electrically driven by a sine wave with the amplitude of 10V. The vibrating fiber surface serves as the mirror in one arm of the interferometer and Doppler-shifts the frequency of the reflected light, yielding spectral side bands spaced at the modulation frequency. Figure 2B is the observed side bands from the cylindrical fiber of Figure 1, driven at frequencies from 1.3 to 1.9 kHz thereby establishing a macroscopic piezoelectric response from the embedded ferroelectric layers. The side band amplitude modulation response is found at ~ -60 dB below the main beat tone around these frequencies.

To improve the signal level, we take advantage of the fact that the fiber drawing process is in a regime dominated by viscous forces thus allowing for cross sections that are far from those dictated by surface energy minimization. A rectangular fiber with an embedded planar piezoelectric layer is produced using a similar technique to the one described above (supplementary online material). The rectangular geometry couples more efficiently to the planar optical beam leading to a marked improvement in the signal measured in the side bands compared to the immediate background as shown in Figure 2C. It also leads to a 10 dB increase in the side band amplitude. The ability to optimize the external fiber geometry with respect to the measurement system and application is another compelling property of this approach.

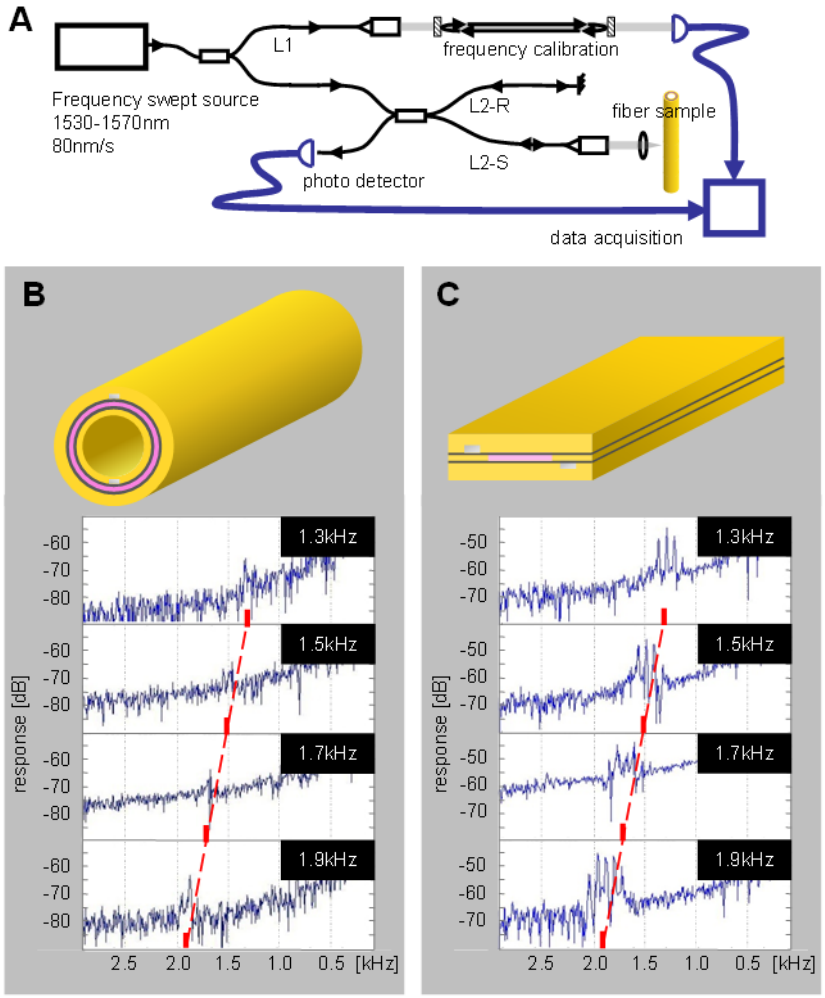

Figure 2 (A) Schematic of the fiber-optic heterodyne interferometer for probing fiber vibration. One of the beam lines (L1) serves as the real-time frequency calibration, to compensate frequency chirp originating from the laser source. The other beam line is further split into two (L2-S and L2-R) in a Michelson interferometer configuration. The line L2-S is focused onto vibrating surface of the fiber sample, and the reflection is recombined and interfered with the line L2-R. (B), (C) The measured side band spectra of the heterodyne beat signals from piezoelectric fibers with cylindrical and rectangular cross sections, respectively.

We follow with direct acoustic measurements, using the fibers both as an acoustic sensor and as an acoustic actuator centered at 1 MHz. Such a frequency range is typical in ultrasound imaging applications. A schematic of the setup is shown in Figure 3A. A water-immersion ultrasonic transducer (Olympus Panametrics-NDT, 1.0 MHz-centered) is coupled to a fiber sample across a water tank to match the acoustic impedance. The fiber sample is attached to the water tank

surface via immersion gel, with the piezoelectric layer facing towards the transducer. The rectangular geometry further improves the acoustic directionality. At MHz frequencies, capacitive electromagnetic coupling between the transducer circuit and the receiver charge amplifier can be significant even with careful shielding and grounding (26). To separate the acoustic signals from the electromagnetic interference, we use a pulsed excitation and time-gate the received signals, exploiting the 5 orders of magnitude difference in the propagation speed between acoustic and electromagnetic pulses. The temporal traces of the amplified voltages under a pulsed excitation are measured with a carrier frequency at 600 kHz and a 52 μs temporal envelope at a 6.5 kHz repetition rate. The time delay of the received pulses is consistent with acoustic propagation in water at 1470 ± 30 m/s (Figure 3B). Frequency domain characterizations of the flat rectangular piezoelectric fibers are performed with a fixed transducer-to-fiber distance, with the pulsed excitation and the time-gated signal processing (Figure 3C). The measured piezoelectric response of the fiber, both as a sensor and an actuator, essentially follows the intrinsic frequency profile of the transducer. Although the frequency range is limited here by the bandwidth of the transducer, polymeric piezoelectric elements are in principle broadband and the piezoelectric fibers could operate at a far broader range of frequencies. For example, similar fibers were used to generate audible sound between 7 kHz and 15 kHz with a driving voltage of 5V.

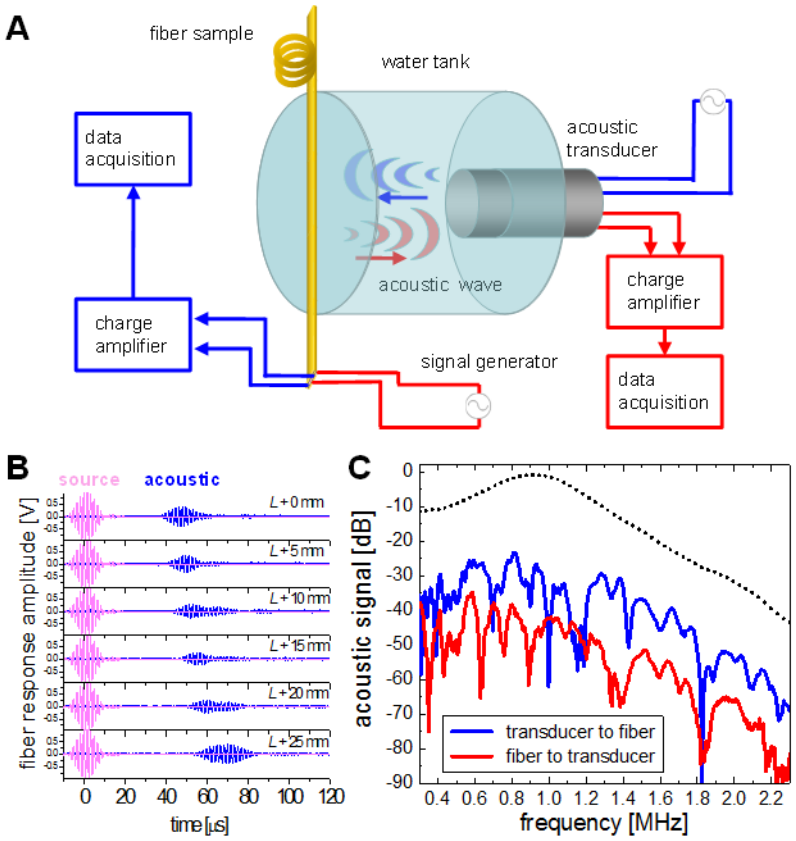

Figure 3 (A) Experimental setup for acoustic characterization of piezoelectric fibers. Acoustic wave travels across a water tank from a water-immersion acoustic transducer to a fiber sample, and vice versa. (B) Temporal traces of electrically-amplified acoustic signals detected by a piezoelectric fiber, shown together with the excitation signals. (C) Acoustic signal detected by a piezoelectric rectangular fiber around 1 MHz. The dotted line is the power spectrum of the (1 MHz-centered) transducer used for excitation.

The potential to modulate sophisticated optical devices is illustrated by constructing a fiber with a Fabry-Perot (FP) optical cavity structure (7, 8) layered on an embedded piezoelectric element. The fabrication process is shown in Figure 4A. SEM images show that the piezoelectric FP rectangular fiber (Figure 4B) is 800 μm wide and exhibits well-maintained preform-to-fiber

dimensional ratio and adhesion of the structures. Reflectivity of the piezoelectric FP fiber is characterized with a Fourier transform infrared (FTIR) microscope (Bruker Optics, Tensor/Hyperion 1000), revealing the reflectivity reaching 90% around 1500 nm (Figure 4C, inset). The spectral dip associated with FP resonant mode is identified at 1550 nm. We again employ heterodyne interferometry to characterize the fiber vibration produced by the embedded piezoelectric element. In Figure 4C, the piezoelectric FP fiber is electrically driven by a sine wave at frequencies stepped from 1.5 through 8.5 kHz at the amplitude of 10V, while the probe beam is focused on the FP structure. The frequency dependence of the side band amplitude suggests signals enhanced or dampened by underlying acoustic resonances of the fiber sample. These piezoelectric FP fibers are mechanically robust and yet flexible; and can be assembled into a fabric for large area coverage as shown in Figure 4D. The manifested color of the fabric is the reflection from the third order band of the Fabry-Perot optical structure embedded in the fibers.

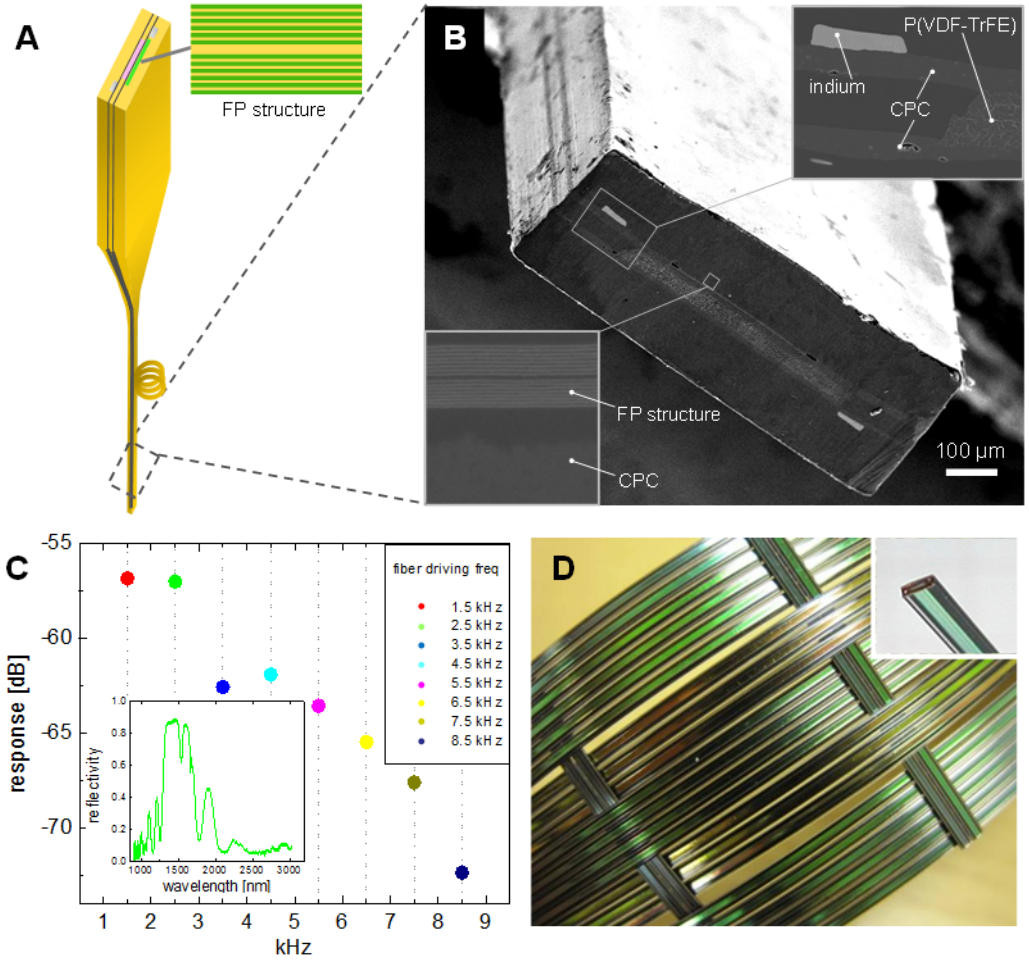

Figure 4 (A) Schematic of the fabrication process of an integrated piezoelectric FP flat rectangular fiber. A FP optical cavity is embedded with the piezoelectric structure in a preform. The preform is thermally drawn into a micro-structured fiber. (B) SEM micrograph of the cross section of an integrated piezoelectric FP fiber. (C) Piezoelectricity of the fiber characterized with the fiber-optic heterodyne interferometer. Inset: Reflection spectrum of the piezoelectric FP fiber measured with FTIR. (D) A two-dimensional device fabric constructed by knitting the piezoelectric/FP fibers as threads. Inset is a photograph of an individual fiber.

The design, fabrication and characterization of extended length of fibers that are piezoelectric transducers is reported. An internal domain comprising a material which crystallizes in the ferroelectric phase is confined by a viscous conductive polymer. These are combined with metal

electrodes to form a macroscopic preform, which is subsequently thermally drawn into many meter length of fibers with well ordered and electrically contacted piezoelectric layers. Excellent uniformity allows for effective poling of the ferroelectric domain at fields exceeding 60MV/m. Piezoelectric response was established across a wide range of frequencies from kHz to MHz ranges using direct acoustic as well as heterodyne optical interferometry setups. By demonstrating monolithic integration of piezoelectric transducers and Fabry-Perot optical resonator in a single fiber, we pave the way toward extending fibers from traditionally passive components to active systems that can be electrically modulated.

References

1. A. F. Abouraddy et al., Nature Mater. 6, 336 (2007).
2. C. Kerbage, A. Hale, A. Yablon, R. S. Windeler, B. J. Eggleton, Appl. Phys. Lett. 79, 3191 (2001).
3. P. Mach et al., Appl. Phys. Lett. 23, 4294 (2002).
4. M.-V. Bergot et al., Opt. Lett. 13, 592 (1988).
5. L. Li, G. Wylangowski, D. N. Payne, R. D. Birch, Electron. Lett. 22, 1020 (1986).
6. M. Folkine et al., Opt. Lett. 27, 1643 (2002).
7. G. Benoit, K. Kuriki, J.-F. Viens, J. D. Joannopoulos, Y. Fink, Opt.Lett. 30, 1620 (2005).
8. G. Benoit, S. D. Hart, B. Temelkuran, J. D. Joannopoulos, Y. Fink, Adv. Mater. 15, 2053 (2003).
9. W. Heywang, K. Lubitz, W. Wersing, Eds., Piezoelectricity: Evolution and Future of a Technology (Springer, Berlin, 2008).
10. J. Curie, P. Curie, C. R. Acad. Sci. 91, 294 (1880).
11. H. S. Nalwa, Ed., Ferroelectric Polymers: Chemistry, Physics, and Applications (M. Dekker, Inc., New York, 1995).
12. A. J. Lovinger, Science 220, 1115 (1983).
13. H. Kawai, Jpn. J. Appl. Phys. 8, 975 (1969).
14. J. B. Lando, H. G. Olf, A. Peterlin, J. Polym. Sci. Part A: Polym. Chem. 4, 941 (1966).
15. K. Matsushige, K. Nagata, S. Imada, T. Takemura, Polymer 21, 1391 (1980).
16. J. Wu, J. M. Schultz, F. Yeh, B. S. Hsiao, B. Chu, Macromolecules 33, 1765 (2000).
17. D. Deng et al., Nano Lett. 8, 4265 (2008).
18. S. D. Hart, Doctoral Thesis, Massachusetts Institute of Technology (2004).
19. T. Furukawa, Phase Trans. 18, 143 (1989).
20. T. Yagi, M. Tatemoto, J. Sako, Polym. J. 12, 209 (1980).
21. J. B. Lando, W. W. Doll, J. Macromol. Sci.-Phys. B2, 205 (1968).
22. K. Koga, H. Ohigashi, J. Appl. Phys. 59, 2142 (1986).
23. K. Kimura, H. Ohigashi, Appl. Phys. Lett. 43, 834 (1983).
24. J. Zheng, Optical Frequency-Modulated Continuous-Wave (FMCW) Interferometry (Springer, New York, 2005).
25. R. Huber, M. Wojtkowski, K. Taira, J. G. Fujimoto, Opt. Express 13, 3513 (2005).
26. R. Morrison, Grounding and Shielding: Circuits and Interference (Wiley-Interscience, Piscataway, NJ, ed. 5th, 2007).